Supplementary Information

Phonon induced near-field effects on heat transfer across nanogap electrodes

Yuki Hanamura, Kazuma Kishimoto, Mizuki Tada, Ryo Yamada,

and Hirokazu Tada

Graduate School of Engineering Science, Osaka University

Machikaneyama 1-3, Toyonaka 560-8531, Japan

Table of Contents

1. Device preparation

The devices were prepared on a silicon substrate with a 100 nm thick silicon nitride (SiN) film obtained from SEIREN KST Corp. Figure S1 shows the device preparation procedure. (a) Metal patterns for electrodes, heaters, thermometers, and actuators were prepared through electron beam lithography (EBL) followed by a lift-off process. An adhesive layer of Chromium (Cr), 5 nm thick, was deposited, succeeded by a 120 nm thick layer of gold (Au). Two electrodes separated by a distance of 400 nm were prepared as the initial gap electrodes. (b) The SiN film was partially removed by reactive ion etching to shape the device. The substrate was exposed to a mixed gas plasma of trifluoromethane (flow rate: 20 sccm) and argon (flow rate: 10 sccm) at 1.3 Pa and 100W for 3.5 minutes using the RIE-10NR (Samco Inc.). (c) Electroplating of Au was applied around the initial gap electrodes to reduce the gap distance. Details of the electroplating process will be described in the following section. (d) Finally, the substrate underwent immersion in an aqueous solution of tetramethylammonium hydroxide (TMAH) (25 wt%, 80°C) to etch away the exposed portion of the silicon substrate, resulting in suspended devices by removing the silicon substrate beneath the bridge-like structure.

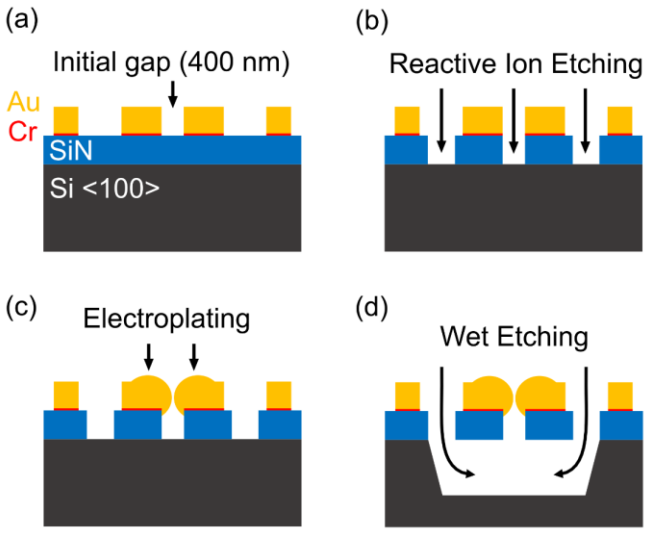

Figure S1. Preparation procedure of the device: (a) Preparation of the metallic patterns including the initial gap electrodes, (b) Etching of the SiN film (c) Electroplating of Au

on the electrodes to reduce the gap distance, and (d) Etching of the silicon substrate with TMAH to form a suspended structure. The diagrams represent cross-sectional views and are not to scale.

2. Preparation of nanogaps by electroplating

Figure S2 shows the experimental setup for electroplating on the nanogap electrodes. The substrate was dipped in a cyanide-based gold plating solution purchased from TANAKA Kikinzoku Kogyo, and a DC current with 50 nA was applied from an anode (100μm × 100μm) to one side (serving as the cathode) of the gap electrodes. Metal structures other than the nanogaps were covered with electron beam resist to protect them from electroplating. The cathode was switched at 30-second intervals to ensure uniform plating of both electrodes forming the gap. A voltmeter monitored the potential difference between the gap electrodes, which dropped to zero when the gap was closed by the deposited gold. During the washing and drying of the substrate, surface tension induced a crack to create a fine nanogap.

Figure S3 shows Scanning Electron Microscope (SEM) images of (a) the lithographically prepared initial electrodes (with an 800 nm gap, for example) and (b, c) the nanogap electrode prepared by the electroplating method. This method enabled the reproducible preparation of nanogap electrodes with a gap spacing of several tens of nanometers. In addition, the resulting electrodes had blunt tips, which provided a wider contact surface, ensuring reliable contact across the gap.

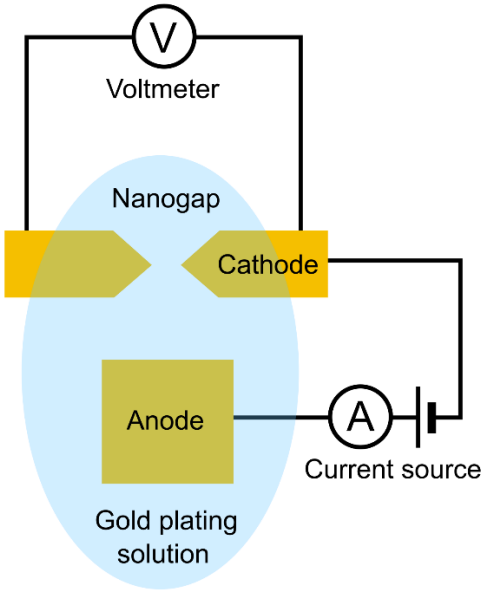

Figure S2. Experimental setup for electroplating on the nanogap electrodes.

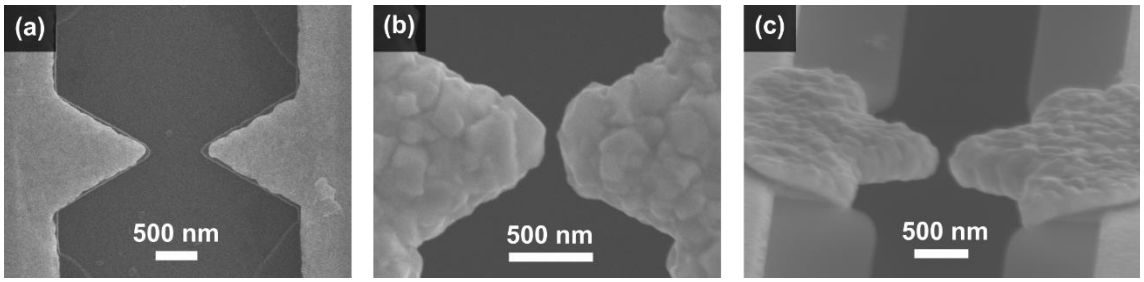

Figure S3. SEM images of (a: top view) the lithographically prepared initial electrodes and (b: top view, c: oblique view) the nanogaps prepared by the electroplating method.

3. Measurement of temperature

When an AC current, $I_{\mathrm{ac}} \sin(\omega t)$, is applied to the heater, an AC heat component, denoted as Q_{ac}, is generated, as described below.

$$Q_{\mathrm{ac}} = \frac{R_{\mathrm{heat}} I_{\mathrm{ac}}^2}{2} \sin\left(2\omega t - \frac{\pi}{2}\right) \tag{S1}$$

where R_{heat} is the resistance of the heater, I_{ac} is the amplitude of the current, ω is the angular frequency of the current, and t is time. At steady state, since both temperature and Q_{ac} oscillate, the temperature oscillation of the heater is described as

$\Delta T_{\mathrm{h}} \sin(2\omega t - \pi/2)$. Similarly, based on the temperature dependence of electrical resistance, the oscillation of the heater resistance, denoted as $R_{\mathrm{heat,ac}}$, is described as follows:

$$R_{\mathrm{heat,ac}} = \Delta T_{\mathrm{h}} \sin\left(2\omega t - \frac{\pi}{2}\right) \cdot \left(\frac{\mathrm{d}R_{\mathrm{heat}}}{\mathrm{d}T}\right) \tag{S2}$$

where $\mathrm{d}R_{\mathrm{heat}}/\mathrm{d}T$ is the temperature coefficient of the resistance of the heater. The AC component of the voltage drop at the heater, $V_{\mathrm{heat,ac}}$, is expressed as:

$$\begin{aligned} V_{\mathrm{heat,ac}} &= \left(R_{\mathrm{heat}} + R_{\mathrm{heat,ac}}\right) I_{\mathrm{ac}} \sin(\omega t) \\ &= R_{\mathrm{heat}}\, I_{\mathrm{ac}} \sin(\omega t) + \frac{\Delta T_{\mathrm{h}} I_{\mathrm{ac}}}{2} \left(\frac{\mathrm{d}R_{\mathrm{heat}}}{\mathrm{d}T}\right) [\sin(\omega t) + \sin(3\omega t - \pi)] \end{aligned} \tag{S3}$$

Denoting the third harmonic component of $V_{\mathrm{heat,ac}}$ as $V_{3\omega}$, the temperature rise of the heater is given by:

$$\Delta T_{\mathrm{h}} = 2 \frac{V_{3\omega}}{I_{\mathrm{ac}}} \left(\frac{\mathrm{d}R_{\mathrm{heat}}}{\mathrm{d}T}\right)^{-1} \tag{S4}$$

The temperature of the sensor can be analyzed similarly to that of the heater. Under steady-state conditions with rapid heat diffusion, the temperature oscillation of the sensor is represented as $\Delta T_{\mathrm{s}} \sin(2\omega t - \pi/2)$. When a DC current, I_{dc}, is applied to the sensor, the AC component of the voltage drop at the sensor, $V_{\mathrm{sens,ac}}$, is described as:

$$V_{\mathrm{sens,ac}} = \Delta T_{\mathrm{s}} I_{\mathrm{dc}} \left(\frac{\mathrm{d}R_{\mathrm{sens}}}{\mathrm{d}T}\right) \sin\left(2\omega t - \frac{\pi}{2}\right) \tag{S5}$$

where $\mathrm{d}R_{\mathrm{sens}}/\mathrm{d}T$ is the temperature coefficient of the resistance of the sensor. Designating the second harmonic component of $V_{\mathrm{sens,ac}}$ as $V_{2\omega}$, the temperature rise of the sensor is expressed as:

$$\Delta T_{\mathrm{s}} = \frac{V_{2\omega}}{I_{\mathrm{dc}}} \left(\frac{\mathrm{d}R_{\mathrm{sens}}}{\mathrm{d}T}\right)^{-1} \tag{S6}$$

Equations S4 and S6 show that the temperatures at both ends of the electrodes can be determined by measuring $V_{3\omega}$ and $V_{2\omega}$ using lock-in amplifiers.

4. Measurement of $V_{3\omega}$

Since the AC component of the voltage drop at the heater in Equation S3 primarily consists of a first-order component, the third harmonic component, $V_{3\omega}$, cannot be measured with commercial lock-in amplifiers due to insufficient dynamic reserve of the input signal. Therefore, $V_{3\omega}$ was isolated using a subtraction circuit employing differential amplifiers. Figure S4 depicts a schematic of the measurement setup, where a bulk resistor is connected in series with the heater. The first-order component was canceled by subtracting the voltage drop across the bulk resistor from that of the heater. Since the bulk resistor has a significantly larger heat capacity compared to the device, the third harmonic component from the resistor can be considered negligible. By adjusting the digital potentiometer to minimize the first-order component, $V_{3\omega}$ was then measured using the lock-in amplifier. This setup enabled automated measurement and tracking of the temperature variation of the heater by computer-controlled adjustment of the potentiometer.

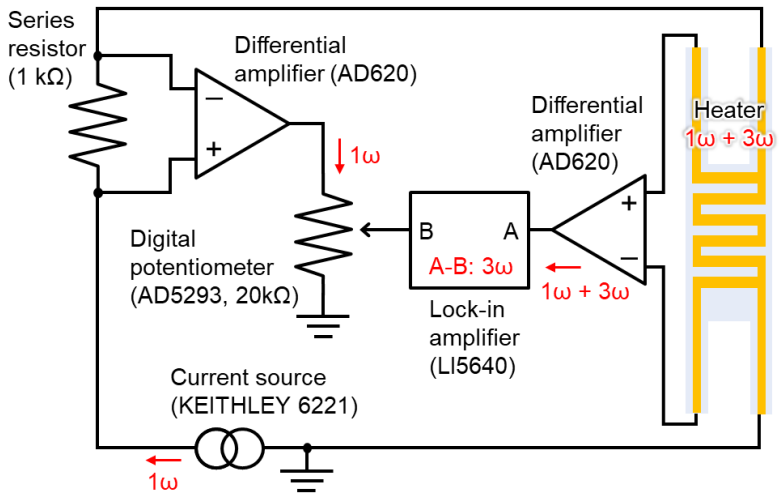

Figure S4. Schematic of the measurement setup for the heater in the device. A KEITHLEY 6221 was used as the AC current source, and a LI5640 (NF Corp.) was used as the lock-in amplifier. The differential amplifier and the digital potentiometer, AD620 and AD5293, respectively, both from Analog Devices Inc., were used to isolate and measure the third harmonic component.

5. Frequency response characteristics of the device

The time dependence of the voltage described in Equations S3 and S5 assumes rapid heat diffusion throughout the device. However, if the frequency of the AC current for heating is too high, heat may not uniformly propagate across the device within a single cycle. This inadequate heat diffusion can cause phase shifts and signal attenuation, compromising the precision of temperature measurements. To determine the appropriate frequency for accurate temperature measurement in the prepared device, the frequency dependence of the phase and amplitude of $V_{3\omega}$ and $V_{2\omega}$ was assessed. Figure S5 (a) illustrates the frequency dependence of the phase. According to Equations S3 and S5, the phases of $V_{3\omega}$ and $V_{2\omega}$ are expected to be $-180°$ and $-90°$, respectively, under conditions of rapid heat diffusion. The measured phase closely matched these theoretical values at frequencies below a few tens of Hertz, with noticeable phase shifts occurring as the frequency increased. Figure S5 (b) illustrates the frequency dependence of amplitude, revealing a nearly constant amplitude for frequencies below 100 Hz but decreased as the frequency increased. Based on these findings, the frequency of the AC current was set to 5 Hz to ensure sufficient margin for phase and amplitude stability.

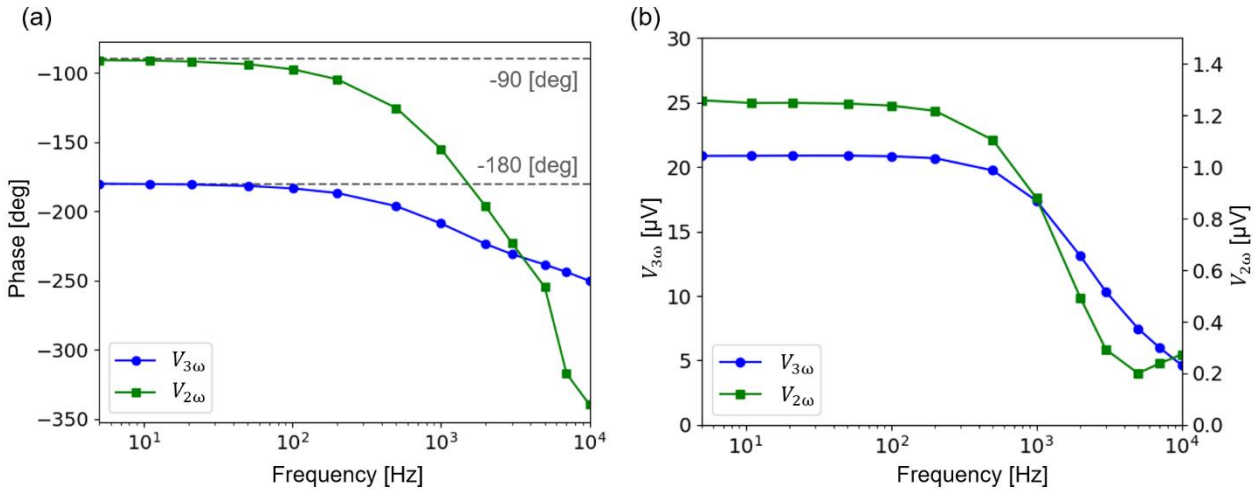

Figure S5. Frequency dependence of the phase (a) and the amplitude (b) of $V_{3\omega}$ (blue) and $V_{2\omega}$ (green).

6. Correction of delay time by lock-in measurement

Due to the presence of a low-pass filter with a significant time constant in the lock-in amplifier, the values obtained from the lock-in measurement are subject to delay. To address this, the time axis of the data was adjusted using the following procedure. A pulse waveform, depicted in Figure S6 (a), represents the amplitude of the AC current, I_{ac}, applied to the heater. Corresponding to this, Figure S6 (b) displays the measured $V_{3\omega}$ signal, which indicate the temperature rise of the heater at that moment. The time constant τ_{c} for $V_{3\omega}$ (the time taken to reach 63.2% of the convergence value) was determined to be 13.5 seconds.

Subsequently, Figure S6 (c) illustrates $V_{3\omega}$ after applying the correction with τ_{c} as the offset on the time axis. Although the waveform appears wider compared to the applied pulse (Figure S6 (a)), this adjustment effectively corrects the deviation in the time axis of the measured values. This correction was applied only to the data in Fig. S12 (Appendix 1). For the real-time lock-in measurements presented in the next section, no correction to the time axis is required.

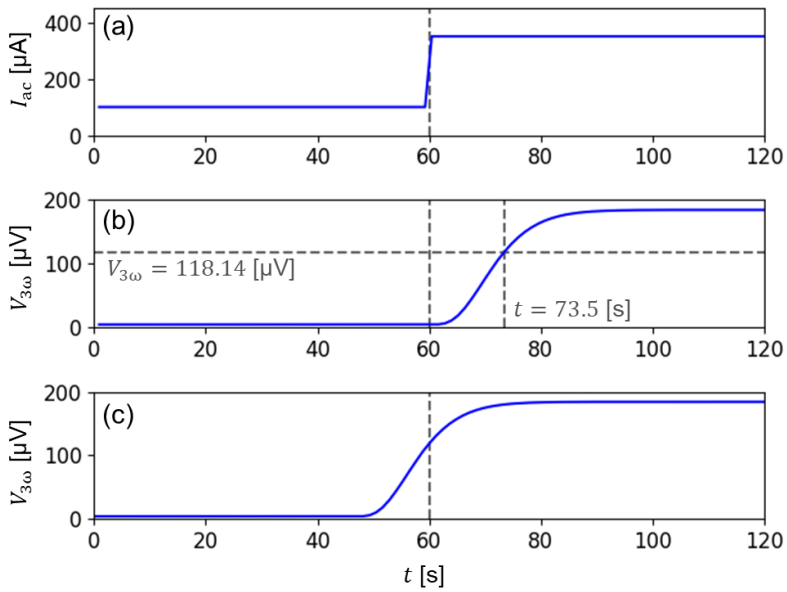

Figure S6. Time lapse of the amplitude of the AC current I_{ac} (a), $V_{3\omega}$ measured with the lock-in amplifier (b), and $V_{3\omega}$ corrected with the time constant of the amplifier (c).

7. Real-time lock-in measurement

As described in Section 6, lock-in measurements at low frequencies using commercial lock-in amplifiers resulted in significant delays on the time axis. To address this, we implemented a real-time lock-in measurement system using digital signal processing, which minimize the delay in the time axis. We replaced the lock-in amplifier with the circuit shown in Figure S7. The input signal (A−B) was amplified 100 times by a differential amplifier (AD620 and AD8429 for $V_{3\omega}$ and $V_{2\omega}$, respectively, both from Analog Devices, Inc.) and then passed through a high-pass filter with a cutoff frequency of 0.08 Hz to remove the DC component. The signal was further amplified by a pre-amplifier (with gains (G) of 10 and 100 for $V_{3\omega}$ and $V_{2\omega}$, respectively), before being input into the data acquisition system (DAQ: NI 9238, National Instruments Corp.). After the computer captured the voltage waveforms obtained by the DAQ, the amplitude and phase of each harmonic component were calculated by fast Fourier transform (FFT). This system enabled us to minimize the time axis delay below 1 second, since the lock-in measurement was completed in a time equivalent to several periods of the signal. The data in Figures 2 − 4 in the main text were obtained using the real-time lock-in measurement system.

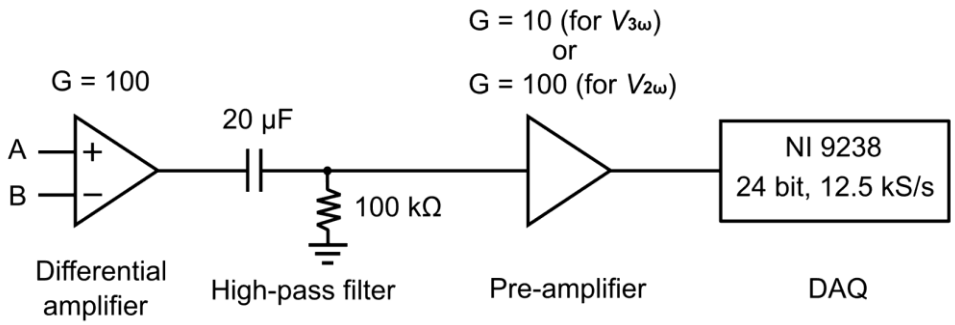

Figure S7. Schematic of the real-time lock-in measurement system.

8. Numerical simulations

Numerical simulations were conducted to support the analysis of measurement results by examining the temperature distribution and deformation within the device. For this purpose, an open-source finite element method solver, Elmer,[S1] was employed.

Figure S8 illustrates the simulated temperature distribution within the device upon applying 1 μW of heat to the heater. Notably, the temperature at the electrode tip was lower than that of the heater, which can be attributed to thermal resistance within the device. In Figure S9 (a), simulated temperatures of the heater, sensor, and both ends of the gap electrode are depicted as a function of the thermal conductance κ_{set} across the gap. The thermal conductance κ obtained from Equation 1 in the main text, is displayed as blue dots in Figure 9 (b). It can be observed that the κ values were lower than κ_{set} (represented by the black line), as per the simulation conditions, indicating a need for correction in Equation 1. When the thermal conductance between the gap falls below a few thousand nW/K, κ exhibits almost linear behavior with respect to κ_{set}, as depicted by the red line. Consequently, once the coefficient η is determined, κ can be adjusted using the following equation:

$$\kappa = \eta \frac{Q\Delta T_{\mathrm{s}}}{\Delta T_{\mathrm{h}}^2 - \Delta T_{\mathrm{s}}^2} \tag{S7}$$

Since the Wiedemann-Franz (WF) law has been reported to hold at the atomic scale in studies on the thermal conductance of thin metal wires,[S2,S3] we derived the coefficient η using the thermal conductance approximated from the electrical conductance of the contact at the nanogap electrode. The experimentally determined values of η were approximately from 1.0 to 2.4.

Although Q in Equation 1 of the main text assumes only the heat generated at the heater, it should also consider heat generated at the leads of the heater for a more accurate estimation of κ. In previous studies using suspended membrane devices, compensation was often performed by adding half of the heat generated at the leads to Q.[S4] This is equivalent to multiplying Equation 1 by a coefficient corresponding to the

resistance ratio of the heater to the leads, which can be integrated into η in Equation S7. In this study, the handling of heat generated at the leads was omitted by the correction using the WF law described above.

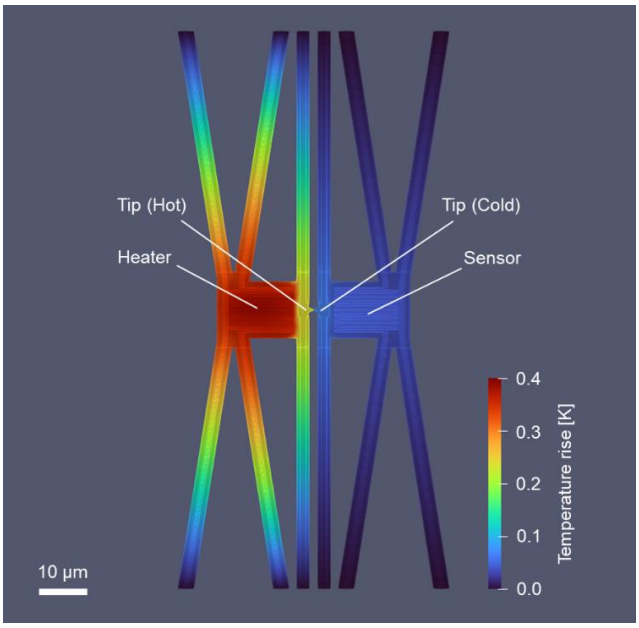

Figure S8. Simulated temperature distribution in the device when the power applied to the heater is 1 μW and thermal conductance through the gap is 10,000 nW/K at 300 K.

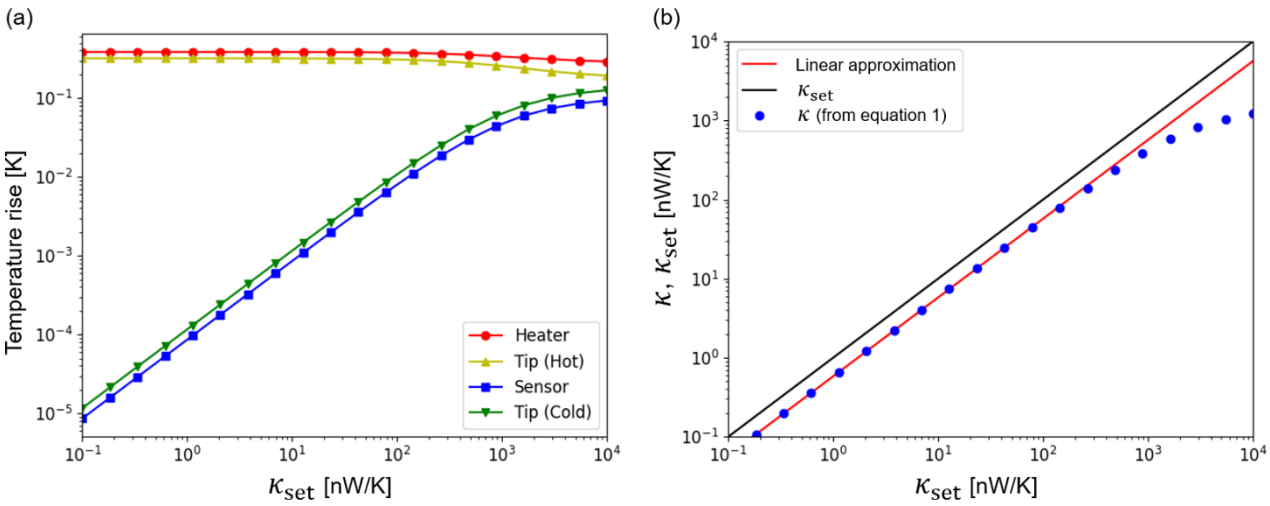

Figure S9. (a) Simulated temperatures of the heater, sensor, and the tip of electrodes as a function of thermal conductance through the gap (κ_{set}). (b) Thermal conductance obtained from Equation 1 in the main text as a function of κ_{set}.

Figure S10 presents the simulation outcomes depicting (a) temperature rise and (b) the deformation of the device under a power input of 200 μW to the actuator. Notably, Figure S10 (b) shows the deformation exaggerated by a factor of 1000. The heating primarily affected the diagonal beams, resulting in concentrated deformation at the electrode tip.

Figure S11 illustrates the displacement of the electrode tip relative to the power applied to the actuator. Remarkably, the displacement exhibited a linear response to the applied power, with an estimated coefficient of 0.054 nm/μW. The coefficients estimated from tunneling current measurements were 0.025 ~ 0.056 nm/μW, demonstrating proximity to the simulated outcome.

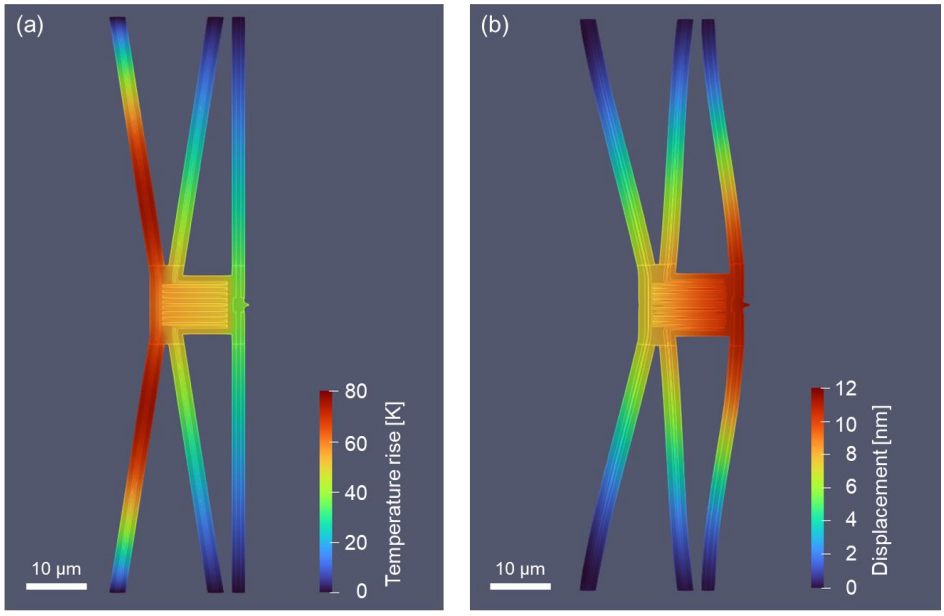

Figure S10. Simulation results of (a) temperature rise and (b) deformation in the device (one side) under the conditions with the power applied to the actuator of 200 μW and the ambient temperature of 300 K.

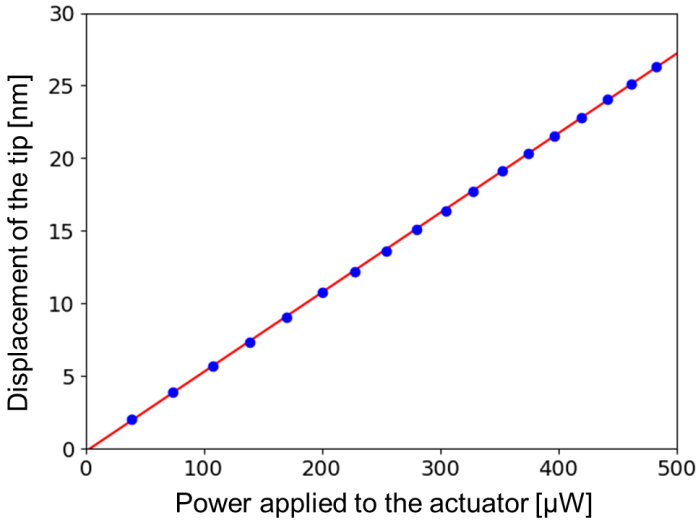

Figure S11. Displacement of the electrode tip as a function of power applied to the actuator (blue dots). A red line indicates linear approximation.

Appendix 1: Thermal conductance of the nanogap prepared by electromigration

While the main text presents heat transfer across the nanogaps prepared by electroplating, we also attempted to create nanogaps from lithographically prepared thin electrodes by electromigration. However, it was challenging to ensure reproducibility due to the low yield of the well-formed nanogaps. The results obtained are shown here for reference. The device preparation procedure will be described in the next section.

Figure S12 shows the gap distance (d) dependence of thermal conductance κ and electrical conductance G for the nanogap prepared by electromigration. Similar to Figure 3 in the main text, an anomalous increase in κ, potentially induced by phonons, was observed at the gap distances as close as a few nanometers. The gap distance dependence of the rising edge of κ followed the relation $\kappa \propto d^{-2.1}$. The difference from the results for nanogaps prepared by electroplating ($\kappa \propto d^{-5}$) suggests that the variations in geometry and surface roughness of the electrodes, due to their preparation methods, impact phonon transport.

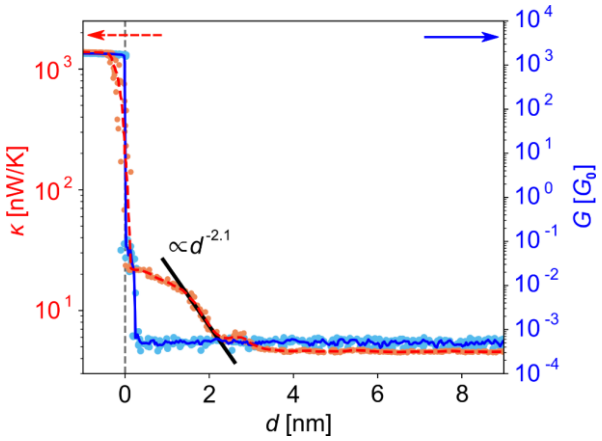

Figure S12. Distance dependence of thermal conductance κ (red, left axis) and electrical conductance G (blue, right axis) as electrodes approach each other. Circular markers represent data points, and the middle lines denote the moving average of the data.

Appendix 2: Device preparation for electromigration

The devices were prepared on a silicon substrate coated with a 100 nm thick SiN film. Figure S13 shows the device preparation procedure. (a) Initially, silicon dioxide (SiO_2) was deposited to coat the SiN film. (b) The SiO_2 layer underwent precise patterning via electron beam lithography (EBL) and subsequent etching with hydrofluoric (HF) acid. (c) The substrate was then immersed in boiling phosphoric acid to etch the SiN film, utilizing the SiO_2 film as a protective mask. (d) To ensure separation of the electrodes from the silicon substrate and prevent contamination by interdiffusion, a sacrificial SiO_2 layer was redeposited prior to electrode preparation. (e) Metal patterns for electrodes, heaters, thermometers, and actuators were prepared through EBL followed by a lift-off process. (f) Finally, the sacrificial layer was dissolved with HF, and the substrate was immersed in tetramethylammonium hydroxide (TAMH, 25 wt%, 80°C) to partly remove the silicon substrate, resulting in a suspended structure. The nanogap was prepared in-situ using electromigration after all lithographic processes. Details on the nanogap preparation will be described in the next section.

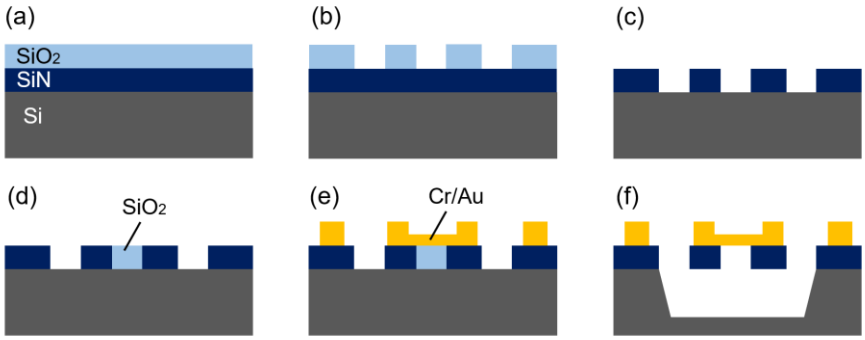

Figure S13. Preparation procedure of the device: (a) Deposition of the SiO_2 film with a thickness of 200 nm, (b) Etching of the SiO_2 film with HF, (c) Etching of the SiN film with phosphoric acid, (d) Deposition of the SiO_2 film as a sacrifice layer, (e) Preparation of the metallic patterns, and (f) Etching of SiO_2 with HF and etching of the silicon substrate with TMAH to form a suspended structure.

Appendix 3: Preparation of the nanogap by electromigration

The nanogap was prepared using electromigration by applying an electric current to a bow-tie-shaped gold electrode. In the conventional electromigration method, the electrode was gradually thinned through feedback-controlled voltage adjustments while monitoring resistance increase.[S5] However, observing resistance changes induced by electromigration in thermally isolated devices was challenging, as the predominant resistance alteration stemmed from temperature elevation due to Joule heating. Our approach capitalized on the near-linear temperature dependence of resistance near room temperature, enabling the detection of nonlinear resistance shifts caused by electromigration through voltage-resistance differentiation, as shown below.

$$\frac{\mathrm{d}R}{\mathrm{d}V} = \frac{R_n - R_{n-1}}{V_n - V_{n-1}} \tag{S8}$$

where $\mathrm{d}R/\mathrm{d}V$ is the differential resistance, R_n is the resistance, V_n is the voltage applied, and n is the number of data points. Figure S14 (a) illustrates the electrode resistance plotted against the applied voltage. Electromigration was detected by

monitoring the derivative $\mathrm{d}R/\mathrm{d}V$ while incrementally increasing the voltage. Upon electromigration detection, the voltage was promptly reduced, then gradually increased again. This stepwise repetition mitigated the risk of electrode breakage due to sudden failure. In Figure S14 (b), the electrical conductance of the electrode is depicted against the number of operation cycles. With increasing cycles, the conductance exhibited a gradual decline. When the conductance reached tens of G_0, the thin electrode underwent spontaneous breakage, leading to the formation of a nanogap electrode. The inset of Figure S14 (b) represents the SEM image of the prepared nanogap. The gap electrodes had smooth surfaces and sharp tips compared to the electroplating method.

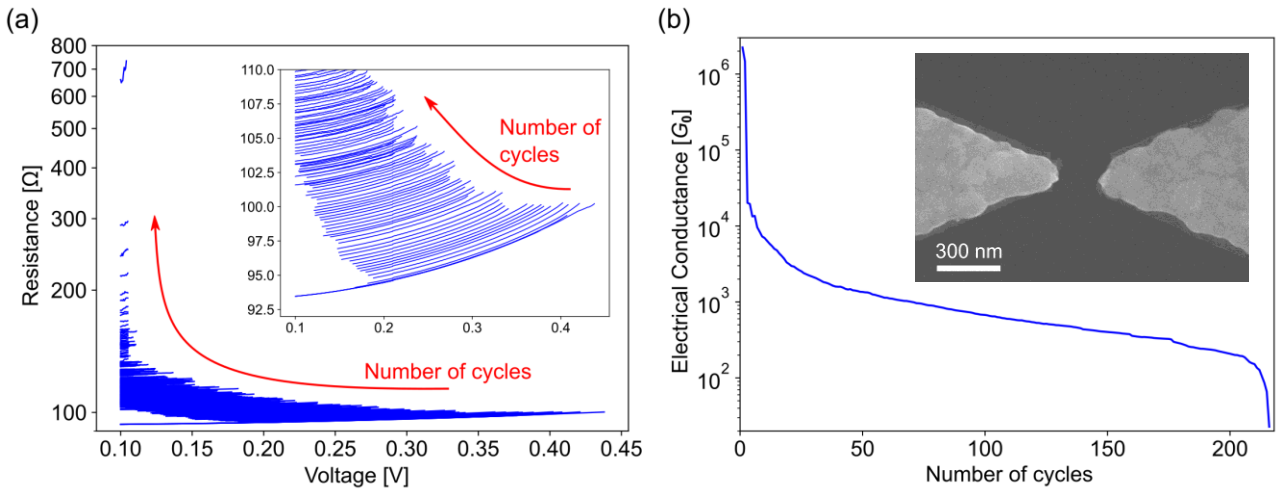

Figure 14. (a) The resistance of the electrode plotted as a function of the voltage applied. Red arrows indicate the direction of increasing electromigration cycles. (b) The electrical conductance of the electrode plotted against the number of electromigration cycles. The inset SEM image depicts the prepared nanogap.

References

S1. Elmer - CSC Company Site, https://research.csc.fi/web/elmer/elmer, (accessed 2024-08-02).

S2. L. Cui, W. Jeong, S. Hur, M. Matt, J. C. Klöckner, F. Pauly, P. Nielaba, J. C. Cuevas, E. Meyhofer, and P. Reddy, *Science* 2017, **355**, 1192–1195.

S3. N. Mosso, A. Prasmusinto, A. Gemma, U. Drechsler, L. Novotny, and B. Gotsmann, *Appl. Phys. Lett.* 2019, **114**, 123102.

S4. J. Y. Wu, W. Wu, and M. T. Pettes, *Rev. Sci. Instrum.* 2016, **87**, 094901.

S5. G. Esen and M. S. Fuhrer, *Appl. Phys. Lett.* 2005, **87**, 263101.